Pharmacokinetics and tumor dynamics of the nanoparticle IT-101 from PET imaging and tumor histological measurements

Thomas Schluep[a], Jungyeon Hwang[a], Isabel J. Hildebrandt[b], Johannes Czernin[b], Chung Hang J. Choi[c], Christopher A. Alabi[c], Brendan C. Mack[c], and Mark E. Davis[c,1]

[a]Calando Pharmaceuticals, Inc., 129 North Hill Avenue, Pasadena, CA 91106; [b]Department of Molecular and Medicinal Pharmacology, David Geffen School of Medicine, University of California, Los Angeles, CA 90095; and [c]Chemical Engineering, California Institute of Technology, Pasadena, CA 91125

Contributed by Mark E. Davis, May 20, 2009 (sent for review April 24, 2009)

IT-101, a cyclodextrin polymer-based nanoparticle containing camptothecin, is in clinical development for the treatment of cancer. Multiorgan pharmacokinetics and accumulation in tumor tissue of IT-101 is investigated by using PET. IT-101 is modified through the attachment of a 1,4,7,10-tetraazacyclododecane-1,4,7-Tris-acetic acid ligand to bind $^{64}Cu^{2+}$. This modification does not affect the particle size and minimally affects the surface charge of the resulting nanoparticles. PET data from ^{64}Cu-labeled IT-101 are used to quantify the in vivo biodistribution in mice bearing Neuro2A s.c. tumors. The ^{64}Cu-labeled IT-101 displays a biphasic plasma elimination. Approximately 8% of the injected dose is rapidly cleared as a low-molecular-weight fraction through the kidneys. The remaining material circulates in plasma with a terminal half-life of 13.3 h. Steadily increasing concentrations, up to 11% injected dose per cm^3, are observed in the tumor over 24 h, higher than any other tissue at that time. A 3-compartment model is used to determine vascular permeability and nanoparticle retention in tumors, and is able to accurately represent the experimental data. The calculated tumor vascular permeability indicates that the majority of nanoparticles stay intact in circulation and do not disassemble into individual polymer strands. A key assumption to modeling the tumor dynamics is that there is a ''sink'' for the nanoparticles within the tumor. Histological measurements using confocal microscopy show that IT-101 localizes within tumor cells and provides the sink in the tumor for the nanoparticles.

cancer | camptothecin | cyclodextrin | polymer | intracellular delivery

Chemotherapeutics are the mainstay of cancer treatment for advanced and/or metastatic tumors. However, their effectiveness is typically limited by toxicity in healthy, normal tissues with rapidly dividing cells, such as bone marrow or the gastrointestinal tract. One approach to increase the therapeutic index of chemotherapeutics is site-directed delivery by using various carrier systems. Numerous types of delivery technologies have been developed for this purpose, such as liposomes (1, 2), conjugates with antibodies or small molecules targeted to tumor antigens (3, 4), and macromolecular polymer carriers (5). Carrier-drug composites are nanoscaled therapeutics, and nanoparticle cancer therapeutics that have been used in humans have been reviewed elsewhere (6).

The use of nanoscaled therapeutics takes advantage of the unique tumor physiology characterized by a high density of abnormal blood vessels, high vascular permeability, and decreased rate of clearance due to a lack of lymphatic drainage, all of which act together to cause accumulation of macromolecules through the enhanced permeability and retention (EPR) effect (7). The magnitude of this effect is affected by a number of parameters that are either host-related (tumor perfusion, vascularity, vascular permeability) or nanoparticle-related (plasma half-life, clearance, hydrodynamic size, surface charge). For example, the hydrodynamic size of macromolecules (or molecular weight, which is directly correlated to hydrodynamic size) appears to be the dominant factor strongly influencing both plasma half-life and vascular permeability. For macromolecules and nanoparticles of <100 nm, plasma half-life is directly correlated, whereas extravasation is inversely correlated, with hydrodynamic diameter (8–12). Surface charge has some effect; e.g., highly cationic polymers show increased clearance compared with those that are negatively or neutrally charged (13). Interestingly, the incorporation of targeting ligands appears to have a minor effect on the biodistribution of nanoparticles to tumors, but may rather affect cellular interactions and therefore improve efficacy for drugs that require intracellular delivery (14, 15). In addition to the EPR effect, nanoscaled carriers improve the pharmacokinetics and pharmacodynamics of small molecule chemotherapeutics through a variety of other mechanisms such as: (*i*) enhancing their solubility and therefore reducing third-spacing, (*ii*) protecting drugs from enzymatic or hydrolytic degradation, (*iii*) controlling release-kinetics to more closely match the mode of action of these drugs, and (*iv*) overcoming multidrug resistance by intracellular delivery through endocytosis rather than diffusion, a process that is less susceptible to surface-pump-mediated multidrug resistance.

Linear, cyclodextrin-based polymers (CDPs) are a unique carrier system for chemotherapeutics and other small molecule drugs (for reviews see refs.16 and 17) because they incorporate β-cyclodextrin, a cyclical sugar with the ability to form inclusion complexes with hydrophobic moieties within the center of its cup-like structure, into a highly water soluble, neutrally charged backbone containing PEG. When small molecule drugs are covalently attached to this polymer through various cleavable linkers, the resulting macromolecular prodrugs self-assemble into nanoparticles with a hydrodynamic diameter of <100 nm. Several conjugates with highly potent small molecule antineoplastic agents have been synthesized and demonstrated enhanced solubility, improved plasma pharmacokinetics, improved tolerability, and increased potency compared with the small molecule analogs (18–22). One nanoparticle that is comprised of a CDP conjugate of the small molecule drug camptothecin (CPT) is named IT-101 (18–21), and is in clinical development (23).

Here, we investigate the transport phenomena of IT-101 (a nanoparticle measuring 30–40 nm in diameter) by using PET. This technology allows the simultaneous and noninvasive measurement of whole-body, multiple-organ pharmacokinetics, in-

Author contributions: T.S., J.C., and M.E.D. designed research; J.H., I.J.H., C.H.J.C., C.A.A., and B.C.M. performed research; T.S., I.J.H., J.C., and M.E.D. analyzed data; and T.S. and M.E.D. wrote the paper.

Conflict of interest statement: M.E.D. was but is no longer a consultant to Calando Pharmaceuticals.

Freely available online through the PNAS open access option.

[1]To whom correspondence should be addressed. E-mail: mdavis@cheme.caltech.edu.

This article contains supporting information online at www.pnas.org/cgi/content/full/0905487106/DCSupplemental.

www.pnas.org/cgi/doi/10.1073/pnas.0905487106

Downloaded at Palestinian Territory, occupied on November 28, 2021

www.manaraa.com

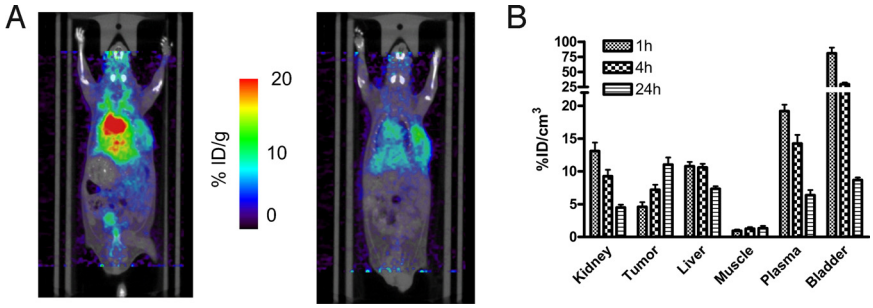

Fig. 1. Results from PET studies. (*A*) Fused PET/CT image of a tumor-bearing mouse 4 h (*Left*) and 24 h (*Right*) after injection. (*B*) Tissue distribution at 1, 4, and 24 h after injection. Error bars indicate SEM.

cluding the distribution to tumors, by using a ^{64}Cu-labeled polymer in tumor-bearing mice. A mathematical model of the nanoparticle behavior is presented and is shown to accurately describe the behavior of IT-101. A key assumption in the model is that there is a "sink" within the tumor for the nanoparticles. Histological sections from tumors evaluated by confocal microscopy show that IT-101 resides within tumor cells and this localization is the sink for the nanoparticles.

Results

Synthesis of ^{64}Cu-Labeled Polymer Conjugate. 1,4,7,10-tetraazacyclododecane-1,4,7-Tris-acetic acid (DOTA) was grafted onto a CDP conjugate of CPT at a molar ratio of 3 CPT to 1 DOTA (*SI Appendix*, Fig. S1). In the resulting conjugate, the DOTA is attached to the polymer through a maleimide linker. The structure of the DOTA-containing polymer conjugate is very similar to that in IT-101. After Cu loading, the resulting polymer conjugate self-assembled into nanoparticles with a similar particle size as IT-101 (37 nm vs. 36 nm, *SI Appendix*, Table S1) and a minor increase in negative surface charge (−9.4 mV vs. −1.8 mV, *SI Appendix*, Table S1). The change in the surface charge can be attributed to the presence of 1 excess carboxylic acid group per DOTA molecule. Cu binding was found to be exclusively through the DOTA groups because no Cu was detected in IT-101 loaded with Cu in the same way (*SI Appendix*, Table S1).

Plasma Pharmacokinetics. MicroPET/CT was used to determine the plasma pharmacokinetics of ^{64}Cu-labeled nanoparticles after i.v. injection in tumor-bearing mice. MicroPET images at 4 h and 24 h after injection are shown in Fig. 1*A*. The PET signal in various organs was measured and the percent of injected dose (ID) per cm^3 for each region of interest was calculated for each time-point. Data for the first 60 min averaged over 6 animals evaluated in 2 independent experiments are provided in the *SI Appendix*, Fig. S2. Plasma and tumor curves expanded to 24 h are shown in Fig. 2*B*. To calculate blood concentration, an area of interest was drawn around the mediastenum. Plasma concentrations were calculated by using a mouse whole-body hematocrit of 33% (24).

Plasma showed a biphasic elimination of PET signal with 4.26% ID/mL cleared with a half-life of 10.6 min whereas 19.9% ID/mL was cleared with a longer half-life of 13.3 h. The calculated volume of the central plasma compartment was 4.1 mL, ≈2.7 times the mouse plasma volume.

Biodistribution and Renal Clearance. Coinciding with the initial plasma clearance phase was a rapid increase in the PET signal in the renal pelvis, which contains the urine collecting ducts. The renal pelvis signal peaked at ≈7.5 min after injection, declining to less than plasma levels at 20 min after administration (*SI Appendix*, Fig. S2). The rapidly clearing fraction of the PET signal accumulated in the bladder as indicated by a rapid bladder-signal rise over the first 20 min, followed by a more gradual increase during the remainder of the first 60 min, to a total signal of 80% ID/mL (*SI Appendix*, Fig. S2). Over the first hour, 8% of injected dose accumulated in the bladder.

Liver and renal cortex PET signals were approximately equal to blood levels over the first 60 min, declining with the same half-life. This seems consistent with the high vascularization of these organs (25, 26), and together with the bladder data seems to indicate that initial and rapid clearance of a small fraction of PET label is mostly through the kidney.

To determine whether nanoparticle formulations contained any low-molecular-weight polymers not incorporated into nanoparticles, we performed membrane fractionation studies (*SI Appendix*, Table S2). No significant fraction of membrane-filterable polymer conjugate was seen below a 100 kDa molecular weight cut-off (MWCO) for a polymer conjugate with an average MW of 67 kDa, whereas a parent polymer with the same MW showed a significant filterable fraction in accordance with its molecular weight. These data indicate that polymer strands are fully incorporated into nanoparticles with no free, low-molecular-weight conjugate present in solution. The nanoparticles were expected to avoid first-pass kidney clearance, because the kidney has a reported MWCO of ≈48 kDa for other polymers such as PEG and dextran (27). However, it is possible that nanoparticle disruption may occur in the blood stream and release of low-molecular-weight conjugates may contribute to the rapidly cleared fraction. Because the imaging technology used here cannot distinguish between intact nanoparticles, individual polymer conjugate strands or ^{64}Cu labels released from the polymer, it remains unknown what form of low-molecular-weight ^{64}Cu is present in the urine.

Signals from the liver (*SI Appendix*, Fig. S2) show that, although concentrations are similar to the levels observed in blood, no accumulation occurs over time. This lack of accumulation may indicate that nanoparticles extravasate from liver sinusoids into the Disse space but are not taken up to a significant degree by resident macrophages or hepatocytes. Extravasation in the liver seems plausible because the fenestrations in liver sinusoids have a diameter of ≈100 nm in the mouse (28). The liver may therefore function as a depot of nanoparticles that can exchange back into circulation. Alternatively, liver clearance of nanoparticles could have identical kinetics to plasma clearance. This result also confirms that there is no significant level of free ^{64}Cu in our nanoparticle preparation, because free ^{64}Cu has been shown to accumulate in the liver over 60 min (15). Biodistribution to other organs such as muscle and brain was low throughout the observation period, confirming that the nanoparticles show low extravasation into normal tissues (except liver) and do not cross the intact blood–brain barrier (19).

Downloaded at Palestinian Territory, occupied on November 28, 2021
www.manaraa.com

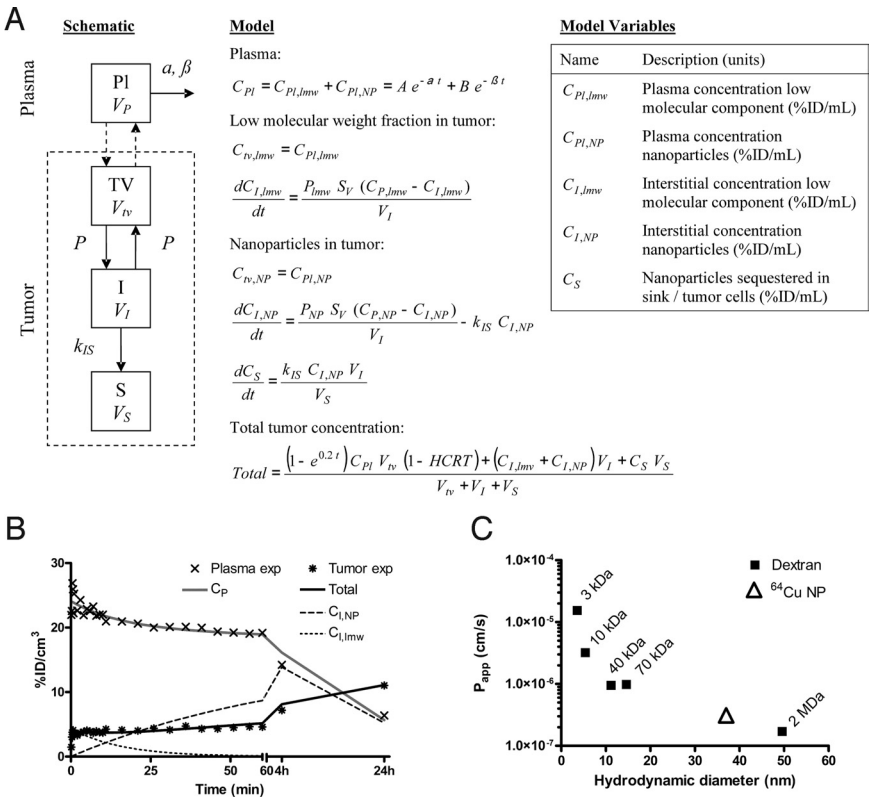

Fig. 2. Modeling of tumor uptake of ^{64}Cu-labeled IT-101 using a 3-compartment model incorporating low molecular weight and nanoparticulate label. (*A*) Schematic diagram and governing equations describing the model. (*B*) Model fit for plasma and tumor concentrations including concentrations in the tumor interstitial space. (*C*) Apparent permeability for IT-101 (denoted ^{64}Cu NP) compared with dextran of varying molecular weight. Dextran was replotted based on data by Dreher et al. (11). See *SI Appendix*, Table S3 for definition of terms and values used in the simulations.

Tumor Accumulation. In contrast to other tissues that exhibit concentration-time curves that declined in parallel with plasma concentration, tumor concentration increased over time, actually crossing above the plasma concentration level at 24 h after injection (Figs. 1*B* and 2*B*). In fact, at 24 h after injection, the PET signal was higher in tumor than in any other tissue, increasing from 4.6 ± 0.7% ID/cm^3 at 1 h to 11.0 ± 1.1%ID/cm^3 at 24 h after injection (Fig. 1*B*).

Compartmental Modeling. Tumor concentration was modeled by using a 3-compartment model (Fig. 2). The initial rapid increase in total tumor concentration is due to the contribution of the tumor vasculature to the total signal. Because plasma and bladder pharmacokinetics indicated the presence of both low-molecular-weight and nanoparticulate ^{64}Cu species, extravasation from tumor vasculature was modeled separately for both. The presence of a low-molecular-weight species of ^{64}Cu leads to a rapid rise of concentration in the tumor interstitial space ($C_{I,lmw}$) that is subsequently cleared with a half-life similar to its plasma half-life (Fig. 2*B*). The apparent permeability for this rapidly clearing ^{64}Cu species was 5.56×10^{-5} cm/s. This apparent permeability is large when compared with the apparent tumor permeability determined by Dreher et al. (11) for a fluorescently labeled dextran with 3.3 kDa molecular weight (1.54×10^{-5}), indicating that it had a molecular weight significantly below 3 kDa. This result is also consistent with the rapid kidney clearance observed in our study, because a copper species <3 kDa is expected to be freely filterable by the kidney.

Tumor interstitial concentration of nanoparticles ($C_{I,NP}$) increased much more slowly, driven by a significantly smaller apparent permeability of 3.1×10^{-7} cm/s. This permeability is consistent with nanoparticles of a 37-nm hydrodynamic diameter but much smaller than what would be expected for a polymer with a molecular weight of 67 kDa (11) (Fig. 2*C*). These results are consistent with the premise that cyclodextrin-based polymer nanoparticles stay intact in circulation for extended periods of time and do not disintegrate into individual polymer strands. Tumor interstitial concentration approaches the plasma concentration by ≈4 h after injection and decreases subsequently in parallel with plasma kinetics. The fact that tumor concentration of label increases above the plasma concentration at some time between 4 and 24 h suggests that there is a sink for the nanoparticles within the tumor; e.g., they become trapped in the tumor tissue or are taken up by cells.

Neuro2A tumors were collected from mice 24 h after injection of IT-101. Sections were visualized by using confocal microscopy because CPT emits at 440 nm (*SI Appendix*, Fig. S3). To prove that the CPT emission was from IT-101 rather than released CPT, we developed a stain for IT-101 (see *SI Appendix* for details of the stain and control experiments proving that it does stain IT-101 in cells). The stain is a gold particle that is capped with thiolated PEG molecules. A portion of these PEG molecules have adamantane (AD) at the end distal to the thiol. Thus, the PEGylated gold particles have numerous AD molecules to provide multivalent binding to the cyclodextrins on the CDP [the AD–CD interactions have been exploited by us previously (15–17)]. Thus, the Au-PEG-AD selectively stains IT-101 (*SI Appendix*). The capped gold particles emit at 507 nm (*SI Appendix*, Fig. S3).

Here, colocalization of CPT and the Au-PEG-AD are used as evidence for IT-101 as opposed to CPT alone. Fig. 3 shows a section of a Neuro2A tumor collected 24 h after injection of IT-101. Note that there is significant colocalization of the

Downloaded at Palestinian Territory, occupied on November 28, 2021
www.manaraa.com

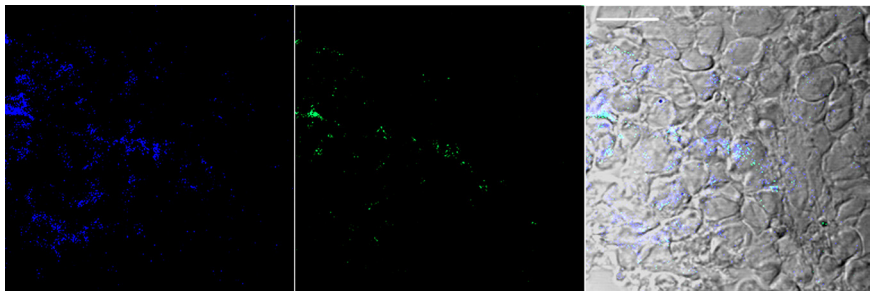

Fig. 3. Confocal immunofluorescence microscopy of Neuro2A tumor section. (*Left*) Emission at 440 nm (blue, CPT). (*Center*) Emission at 507 nm (green, Au-PEG-AD). (*Right*) Merged image of *Left* and *Center* with brightfield image. Scale bar, 20 microns.

emissions from the CPT and the Au-PEG-AD, suggesting that numerous cancer cells within the tumor have internalized IT-101.

Discussion

In this study we used PET to determine multiorgan pharmacokinetics and biodistribution of a nanoparticle containing the chemotherapeutic camptothecin in tumor-bearing mice. Essentially, real-time whole-body data for the first 60 min and additional, discontinuous data up to 24 h after administration were obtained. These data provide for the observation of fast dynamics and give insights into the behavior of the polymeric nanoparticle system that are not possible from other methodologies. The PET dynamics complement PK and biodistribution data acquired at larger time intervals by traditional means.

Self-assembly of multiple polymer chains via inter-strand CD–CPT inclusion complex formation (each polymer strand is a multivalent polymer strand) to create nanoparticles is a unique feature of the cyclodextrin polymer conjugates. The assembly is not limited to CPT (IT-101) as other conjugated molecules also allow for nanoparticle formation (22).

Modification of the CDP–CPT conjugate with DOTA resulted in a structure similar to IT-101, which is currently in clinical trials for the treatment of cancer. After loading with ^{64}Cu, the conjugate assembled into nanoparticles with a particle size of 37 nm and slightly negative surface charge similar to what is observed from IT-101. Plasma pharmacokinetics displayed a biphasic elimination profile with a low-molecular-weight fraction cleared rapidly through the kidneys and the remaining nanoparticles circulating with a terminal half-life of ≈13 h. These results are consistent with previous IT-101 data in rats where the terminal half-life was 18 h (19). The nature of the rapidly clearing low-molecular-weight species could not be determined. However, it is unlikely to be due to the presence of free copper, because none was detected in the starting materials, and injected free copper was shown to accumulate in the liver, rather than being excreted in the urine (15). Possible other explanations include the release of low-molecular-weight polymer conjugates from the nanoparticles after i.v. injection or cleavage of the DOTA ligand from the complex. Copper-loaded DOTA has previously been shown to be renally cleared (15). Cleavage of alkyl-maleimide linkers, as used here, has been reported in plasma, however, the half-life was generally on the order of weeks, not minutes (29), making this hypothesis relatively unlikely.

Biodistribution of the conjugate was also consistent with previous data on IT-101 where the highest tissue concentration at 24 h after administration was observed in tumor, followed by the liver (19). High liver concentrations are most likely a reflection of the accessibility of the liver interstitial space to the nanoparticles through fenestrae with a size of 100 nm. However, the lack of accumulation in the liver together with the low volume of distribution and long terminal half-life indicates that the IT-101 nanoparticles can successfully avoid significant uptake by the reticulo-endothelial system and clearance by the liver.

Tumor permeability of macromolecules, and therefore their extravasation, is expected to decrease with increasing particle size. This is due to the size of the large, intercellular openings between endothelial cells in tumor vasculature that is not present in normal, continuous endothelium (30). The pore cut-off size for these openings has been shown to be between 200 nm and 1.2 μm (9), varying by tumor type. The determined apparent permeability for IT-101 was significantly smaller than the permeability of a 70-kDa dextran polymer but larger than that of a 2-MDa dextran. Additionally, Dreher et al. (11) found that for a 70-kDa dextran, the tumor interstitial concentration reaches a maximum at ≈15 min after injection (the maximum concentration was not experimentally determined for the 2 MDa dextran). In contrast, interstitial concentrations of IT-101 continued to increase up to 4 h after injection. The dynamics of IT-101 tumor accumulation therefore indicate that the majority of the nanoparticles stay intact in circulation and do not disassemble into individual 67-kDa polymer strands to a significant degree. Although IT-101 exhibited a low permeability, this was clearly compensated by a long plasma half-life, leading to a high tumor accumulation. These data demonstrate the EPR effect, with tumor concentration increasing gradually up to 24 h, reaching 11% ID/cm^3, the highest concentration of any tissue.

The observation that tumor concentrations continued to increase above the plasma concentration indicates significant retention of nanoparticles. Several mechanisms have been proposed for nanoparticle retention in tumors: Moore et al. found that dextran-coated iron oxide nanoparticles accumulated in the interstitial fluid, extracellular space, and were taken up by tumor vascular endothelial cells, tumor-associated macrophages (TAM), and tumor cells in a mouse glioma model (31). Uptake by tumor endothelial cells was mostly observed in areas of neovascularization whereas intracellular concentrations were highest in tumor cells. Kirpotin et al. (14) showed that long circulating liposomes accumulated predominantly in tumor stroma, either in the extracellular space or in TAM in a breast cancer tumor model. A Her2-targeted version of the same liposomes achieved the same over all tumor concentration but more internalization by cancer cells through endocytosis was observed. CDP conjugates have been shown to be avidly taken up by cancer cells (18). This result may be a function of the unique surface characteristics of CDP nanoparticles, which contain hydrophobic pockets within the cyclodextrin molecules that have been shown to interact with lipid rafts of cell membranes (16). Although the PET data are not able to distinguish the individual contributions of each of these mechanisms to tumor retention of IT-101, it is important to note that a combination of any of these could contribute to the superior antitumor efficacy seen in preclinical models (18, 20, 21). For

Downloaded at Palestinian Territory, occupied on November 28, 2021

www.manaraa.com

example, uptake by endothelial cells in an area of neovascularization could have an anti-angiogenic effect, starving the tumor of new blood supply. Entrapment in the perivascular extracellular space could lead to a continuous release of drug from the polymer through hydrolytic and enzymatic cleavage, and subsequent transport of free drug to tumor cells by diffusion along a concentration gradient. Uptake by cancer cells could lead to intracellular release of drugs, leading to higher intracellular tumor concentrations than could be achieved otherwise.

To ascertain the localization of IT-101 within the tumors of the mice, Neuro2A tumors were collected 24 h after injection of IT-101. As shown by the confocal immunofluorescence data of Fig. 3, IT-101 is found internalized within tumor cells (Fig. 3 is representative of numerous sections obtained). Because of the significant colocalization of CPT and the Au-PEG-AD that binds to cyclodextrins, it is clear that IT-101 is within the tumor cells and not just released CPT. This localization suggests that the sink for IT-101 within the tumor is the uptake of the nanoparticles by the tumor cells. Tumor cell uptake of IT-101 could be the reason why the tumor amounts of both the IT-101 nanoparticles and CPT remain relatively constant for several days after an i.v. injection as opposed to the rapid decline (over several orders of magnitude in $<$24 h) of irinotecan in the same animal model (21).

In summary, this study highlights the behavior of long-circulating nanoparticles that are able to accumulate in tumor tissue through the EPR effect and result in a selective accumulation in tumor tissue compared with other tissues. Once accumulated in tumor tissue, the nanoparticles are able to enter tumor cells. These combined properties are advantageous for delivery of drugs that require intracellular localization for efficacy. Specific examples of importance would be the delivery of chemotherapeutic agents to tumors resistant to therapy mediated by surface protein pumps and the delivery of nucleic acids.

Materials and Methods

General. All of the anhydrous solvents, HPLC grade solvents, and other common organic solvents were purchased from commercial suppliers and used without further purification. CPT was purchased from Boehringer Ingelheim. Linear copolymer of cyclodextrin and polyethylene glycol (CDP) and the glycine derivative of CPT (TFA Glycinate CPT) were synthesized as previously described (32). Molecular weight distributions of the polymer samples were analyzed on a Wyatt WinGPC Unity system, coupled with double gel permeation columns (PL-aquagel-OH-40, 8 μm, 300 $\times$ 7.5 mm, Polymer Laboratories) on a HP 1100 HPLC system (Agilent). Particle size measurement by dynamic light scattering and zeta potential determinations were performed on a ZetaPALS instrument (Brookhaven Instruments).

Synthesis of CDP-CPT$_3$-SSPyr$_1$. CDP (2.0 g, 0.41 mmol) was dissolved in dry N,N-dimethylformamide (20 mL). The mixture was stirred for 20 min. TFA Glycinate CPT (350 mg, 0.68 mmol), S-(2-Pyridyldithio) cysteamine hydrochloride (51 mg, 0.23 mmol), N,N-Diisopropylethylamine (0.16 mL, 0.91 mmol), *N*-(3-Dimethylaminopropyl)-N′-ethylcarbodiimide hydrochloride (240 mg, 1.2 mmol), and *N*-Hydroxysuccinimide (100 mg, 0.91 mmol) were added to the polymer solution and stirred for 4 h. The polymer was precipitated with acetone (100 mL). The precipitate was dissolved in pH 3 water (100 mL) that was prepared by acidification with HCl. The solution was dialyzed by using a 25,000 MWCO membrane (Spectra/Por 7) for 24 h at pH 3 water. It was filtered through 0.2-μm filters (Nalge) and lyophilized to yield yellow solid (1.1 g, 55%).

Synthesis of CDP-CPT$_3$-SH$_1$. To a PBS (1x, pH 7.4) solution of CDP-CPT$_3$-SSPyr$_1$ (200 mg, 0.036 mmol), DTT (28 mg, 0.18 mmol) was added. The reaction mixture was stirred for 4 h. It was then dialyzed by using a 25,000 MWCO membrane (Spectra/Por 7) for 24 h against a degassed aqueous solution of EDTA (EDTA 1 mM, 2 L). After filtration through a 0.2-μm filter membrane, the solution was lyophilized to produce a light-yellow solid (160 mg, 80%).

Synthesis of CDP-CPT$_3$-DOTA$_1$. CDP-CPT$_3$-SH$_1$ (100 mg, 0.018 mmol) was dissolved in dry N,N-dimethylformamide (2 mL). The mixture was stirred for 20 min. 1,4,7,10-Tetraazacyclododecane-1,4,7-Tris-acetic acid-10-maleimidoethylacetamide (18 mg, 0.022 mmol) was added to the polymer solution and stirred for 15 h. The polymer was precipitated with acetone (10 mL). The precipitate was dissolved in pH 3 water (10 mL) that was prepared by acidification with HCl. The solution was dialyzed by using a 25,000 MWCO membrane (Spectra/Por 7) for 24 h at pH 3 water. It was filtered through 0.2-μm filters (Nalge) and lyophilized to yield yellow solid (68 mg, 68%). Loading of CPT was determined to be a total of 4.9% with 0.1% free CPT per total CPT by HPLC as previously described (32).

Determination of Cu Loading. CDP-CPT$_3$-DOTA$_1$ (20 mg, 0.0036 mmol) was dissolved in 0.1 M ammonium acetate at pH 5.5 (2 mL). Copper (II) chloride (240 μg, 1.7 μmol) was added to the polymer solution and stirred at 60 °C for 3 h. Buffer was exchanged to phosphate buffer at pH 7.4 by using Pierce Zeba 5 mL Desalt spin columns according to the manufacturer's procedure, as follows: Phosphate buffer (2.5 mL) was added to the column and centrifuged at 1,000 $\times$ *g* for 2 min to remove buffer. This buffer-washing procedure was repeated 3 more times. Copper polymer conjugate solution (2 mL) was loaded to the column and centrifuged at 1,000 $\times$ *g* for 2 min to obtain the sample. Samples were analyzed for copper content by inductively coupled plasma mass spectrometry (Galbraith Laboratories).

^{64}Cu Labeling. All liquids were pretreated with Chelex-100 (Bio-Rad) to remove trace metal contaminants. ^{64}Cu chloride was purchased from MDS Nordion and the labeling procedure was performed similar the Cu loading described above, except that the incubation was only for 1 h. The labeling yield was determined by measuring the radioactivity in the filter, the filtrate, and the retentate, respectively. The ^{64}Cu-radiolabeled nanoparticles were then resuspended in saline for in vivo injections.

Animals and Tumor Formation for PET Studies. Nonobese diabetic (NOD)/SCID mice were purchased from Jackson Laboratory. All animal protocols were performed in accordance to the Guide for Care and Use of Laboratory Animals and were approved by the University of California at Los Angeles Animal Research Committee. Neuro2A mouse neuroblastoma cells (ATCC) were cultured in DMEM supplemented with 10% FBS, 2 mg/mL glucose, 100 units/mL penicillin, and 100 units/mL streptomycin. Cells were harvested with trypsin, resuspended in PBS and Matrigel (BD Biosciences), and 1 to 2 million cells were injected s.c. into the right flank of NOD/SCID mice. Tumors were allowed to grow to a size of $\approx$0.5 cm^3 before injection and imaging.

MicroPET CT Imaging. MicroPET/CT imaging was performed on a microPET Focus 220 PET scanner (Siemens) and a MicroCat II CT scanner (Siemens) as previously described (13). Briefly, anesthetized animals were placed in a heated isolation/imaging chamber, positioned on the scanner bed, ^{64}Cu-labeled nanoparticles (100–300 μCi, 1 Ci = 37 GBq) were injected via tail vein, and a dynamic PET scan was acquired for 1 h with an image resolution of 1.7 mm. Immediately after the microPET scan, mice underwent a microCT scan that was used for anatomical localization of the PET signal. Static microPET/CT scans were acquired at 4 h and 24 h after injection. Tracer concentration in various tissues was determined by using the AMIDE software (33). Activity concentrations are expressed as percent of decay-corrected injected activity per cm^3 of tissue (approximately %ID/cm^3), normalized to an elliptic cylinder region of interest drawn over the entire mouse. Plasma concentrations were calculated from measured whole-blood concentrations by using a hematocrit of 33%.

Animals and Tumor Formation for Tumor Collections. Immunodeficient (NOD.CB17-Prkdcscid/J) mice were purchased from The Jackson Laboratory. All animal manipulations, performed with sterile techniques, complied with the National Institutes of Health Guidelines for Animal Care and were performed as approved by the Caltech Institutional Animal Care and Use Committee. Neuro2A cells were cultured in complete growth medium (DMEM supplemented with 10% FBS (FBS), 100 units per mL penicillin, and 100 units per mL streptomycin). In the right hind flank, mice received a s.c. implantation of Neuro2A cells (at 1 million cells per mouse per 0.1 mL of DMEM). Before injection, tumors reached 100–200 mm^3 in size, as determined by caliper measurements. Mice received i.v. administration of IT-101 (10 mg of polymer per kg of animal; formulated in 0.1 mL of D5W) via the tail vein. As a control, mice received i.v. injections of 0.1 mL of D5W. Animal euthanization by CO_2 took place 24 h after injection, immediately followed by tumor extraction.

Confocal Immunofluorescence Microscopy. After immersion fixation in 4% paraformaldehyde for 3 days, 2-cm^3 tumor tissue blocks passed through an

Downloaded at Palestinian Territory, occupied on November 28, 2021
www.manaraa.com

increasing sucrose gradient up to 30% sucrose, and were later embedded in 9% gelatin. The gradual freezing of gelatin tissue blocks to −80 °C allowed the generation of 10 μm-thick cryosections. After brief rinsing with PBS to remove any surface gelatin, as well as fixation with acetone at −20 °C to permeabilize the cell membrane, tissue sections received the staining of PEGylated, AD-modified gold nanoparticles (Au-PEG-AD) in the dark for 2 h. Rinsing with PBS removed any nonspecifically bound gold particles before the mounting of Au-PEG-AD-stained tumor sections with Mowiol 4–88 and glycerol. A Zeiss LSM 510 confocal scanning microscope was used to collect the images (CPT-excitation: 370 nm, emission: 440 nm; Au-PEG-AD-excitation: 488 nm, emission: 507 nm).

ACKNOWLEDGMENTS. This work was supported in part by the National Cancer Institute Grant CA 119347.

1. Torchilin VP (2005) Recent advances with liposomes as pharmaceutical carriers. *Nat Rev Drug Discov* 4:145–160.
2. Drummond DC, Meyer O, Hong K, Kirpotin DB, Papahadjopoulos D (1999) Optimizing liposomes for delivery of chemotherapeutic agents to solid tumors. *Pharmacol Rev* 51:691–743.
3. Carter PJ, Senter PD (2008) Antibody-drug conjugates for cancer therapy. *Cancer J* 14:154–169.
4. Reddy JA, et al. (2007) Preclinical evaluation of EC145, a folate-vinca alkaloid conjugate. *Cancer Res* 67:4434–4442.
5. Tong R, Cheng J (2007) Anticancer Polymeric Nanomedicines. *Polymer Reviews* 47:345–381.
6. Davis ME, Chen ZG, Shin DM (2008) Nanoparticle therapeutics: An emerging treatment modality for cancer. *Nat Rev Drug Discov* 7:771–782.
7. Matsumura Y, Maeda H (1986) A new concept for macromolecular therapeutics in cancer chemotherapy: Mechanism of tumoritropic accumulation of proteins and the antitumor agent SMANCS. *Cancer Res* 46:6387–6392.
8. Tabata Y, Murakami Y, Ikada Y (1998) Tumor accumulation of poly(vinyl alcohol) of different sizes after intravenous injection. *J Control Release* 50:123–133.
9. Hobbs SK, et al. (1998) Regulation of transport pathways in tumor vessels: Role of tumor type and microenvironment. *Proc Natl Acad Sci USA* 95:4607–4612.
10. Yuan F, et al. (1995) Vascular permeability in a human tumor xenograft: Molecular size dependence and cutoff size. *Cancer Res* 55:3752–3756.
11. Dreher MR, et al. (2006) Tumor vascular permeability, accumulation, and penetration of macromolecular drug carriers. *J Natl Cancer Inst* 98:335–344.
12. Perrault SD, Walkey C, Jennings T, Fischer HC, Chan WC (2009) Mediating tumor targeting efficiency of nanoparticles through design. *Nano Lett* 9:1909–1915.
13. Tabata Y, Kawai T, Murakami Y, Ikada Y (1997) Electric charge influence of dextran derivatives on their tumor accumulation after intravenous injection. *Drug Delivery* 4:213–221.
14. Kirpotin DB, et al. (2006) Antibody targeting of long-circulating lipidic nanoparticles does not increase tumor localization but does increase internalization in animal models. *Cancer Res* 66:6732–6740.
15. Bartlett DW, Su H, Hildebrandt IJ, Weber WA, Davis ME (2007) Impact of tumor-specific targeting on the biodistribution and efficacy of siRNA nanoparticles measured by multimodality in vivo imaging. *Proc Natl Acad Sci USA* 104:15549–15554.
16. Davis ME, Brewster ME (2004) Cyclodextrin-based pharmaceutics: Past, present and future. *Nat Rev Drug Discov* 3:1023–1035.
17. Heidel JD (2006) Linear cyclodextrin-containing polymers and their use as delivery agents. *Expert Opin Drug Deliv* 3:641–646.
18. Cheng J, Khin KT, Davis ME (2004) Antitumor activity of beta-cyclodextrin polymer-campthothecin conjugates. *Mol Pharm* 1:183–193.
19. Schluep T, Cheng J, Khin KT, Davis ME (2006) Pharmacokinetics and biodistribution of the camptothecin-polymer conjugate IT-101 in rats and tumor-bearing mice. *Cancer Chemother Pharmacol* 57:654–662.
20. Schluep T, et al. (2006) Preclinical efficacy of the camptothecin-polymer conjugate IT-101 in multiple cancer models. *Clin Cancer Res* 12:1606–1614.
21. Numbenjapon T, et al. (2009) Preclincal results of camptothecin-polymer conjugate (IT-101) in multiple human lymphoma xenograft models. *Clin Cancer Res*, in press.
22. Schluep T, et al. (2009) Polymeric tubulysin-peptide nanoparticles with potent antitumor activity. *Clin Cancer Res* 15:181–189.
23. Oliver JC, Yen Y, Synold T, Schluep T, Davis ME (2008) A dose-finding pharmacokinetic study of IT-101, the first de novo designed nanoparticle therapeutic, in refractory solid tumors. *J Clin Oncol* 26:14538 (abstr).
24. Riches AC, Sharp JG, Thomas DB, Smith SV (1973) Blood volume determination in the mouse. *J Physiol* 228:279–284.
25. O'Connor SW, Bale WF (1984) Accessibility of circulating immunoglobulin G to the extravascular compartment of solid rat tumors. *Cancer Res* 44:3719–3723.
26. Tirona RG, Schwab AJ, Geng W, Pang KS (1998) Hepatic clearance models: Comparison of the dispersion and Goresky models in outflow profiles from multiple indicator dilution rat liver studies. *Drug Metab Dispos* 26:465–475.
27. Jorgensen KE, Moller JV (1979) Use of flexible polymers as probes of glomerular pore size. *Am J Physiol* 236:F103–F111.
28. Braet F, Wisse E (2002) Structural and functional aspects of liver sinusoidal endothelial cell fenestrae: A review. *Comp Hepatol* 1:1.
29. Alley SC, et al. (2008) Contribution of linker stability to the activities of anticancer immunoconjugates. *Bioconj Chem* 19:759–765.
30. Hashizume H, et al. (2000) Openings between defective endothelial cells explain tumor vessel leakiness. *Am J Pathol* 156:1363–1380.
31. Moore A, Marecos E, Bogdanov A, Jr, Weissleder R (2000) Tumoral distribution of long-circulating dextran-coated iron oxide nanoparticles in a rodent model. *Radiology* 214:568–574.
32. Cheng J, Khin KT, Jensen GS, Liu A, Davis ME (2003) Synthesis of linear, beta-cyclodextrin-based polymers and their camptothecin conjugates. *Bioconj Chem* 14:1007–1017.
33. Loening AM, Gambhir SS (2003) AMIDE: A free software tool for multimodality medical image analysis. *Mol Imaging* 2:131–137.

Downloaded at Palestinian Territory, occupied on November 28, 2021

www.manaraa.com